Biomedical Optics EXPRESS

Analysis of skin lesions using laminar optical tomography

Timothy J. Muldoon,[1,3,*] Sean A. Burgess,[1,3] Brenda R. Chen,[1] Désirée Ratner,[2] and Elizabeth M. C. Hillman[1]

[1]*Laboratory for Functional Optical Imaging, Departments of Biomedical Engineering and Radiology, Columbia University, New York, NY 10027, USA*
[2]*Department of Dermatology, Columbia University Medical Center, New York, NY 10027, USA*
[3]*Equal contribution from both authors*
**tjm2145@columbia.edu*

Abstract: Evaluation of suspicious skin lesions by dermatologists is usually accomplished using white light examination and direct punch or surgical biopsy. However, these techniques can be imprecise for estimating a lesion's margin or level of dermal invasion when planning surgical resection. Laminar optical tomography (LOT) is an imaging technique capable of acquiring depth-sensitive information within scattering tissues. Here, we explore whether LOT data can be used to predict the depth and thickness of pigmented lesions using a range of simulations and phantom models. We then compare these results to LOT data acquired on normal and malignant skin lesions *in vivo*.

OCIS codes: (170.3880) Medical and biological imaging; (170.3890) Medical optics instrumentation.

References and links

1. H. W. Rogers, M. A. Weinstock, A. R. Harris, M. R. Hinckley, S. R. Feldman, A. B. Fleischer, and B. M. Coldiron, "Incidence estimate of nonmelanoma skin cancer in the United States, 2006," Arch. Dermatol. **146**(3), 283–287 (2010).
2. N. A. Howlader, N. M. Krapcho, N. Neyman, R. Aminou, S. F. Altekruse, C. L. Kosary, J. Ruhl, Z. Tatalovich, H. Cho, A. Mariotto, M. P. Eisner, D. R. Lewis, H. S. Chen, E. J. Feuer, and K. A. Cronin, eds., *SEER Cancer Statistics Review, 1975-2009 (Vintage 2009 Populations)*, (National Cancer Institute, Bethesda, MD, 2012).
3. J. A. Neville, E. Welch, and D. J. Leffell, "Management of nonmelanoma skin cancer in 2007," Nat. Clin. Pract. Oncol. **4**(8), 462–469 (2007).
4. J. Cook, "Surgical margins for resection of primary cutaneous melanoma," Clin. Dermatol. **22**(3), 228–233 (2004).
5. J. G. A. M. de Visscher, P. J. J. Gooris, A. Vermey, and J. L. N. Roodenburg, "Surgical margins for resection of squamous cell carcinoma of the lower lip," Int. J. Oral Maxillofac. Surg. **31**(2), 154–157 (2002).
6. M. G. O'Rourke and C. Bourke, "Recommended width of excision for primary malignant melanoma," World J. Surg. **19**(3), 343–345 (1995).
7. R. S. Batra and L. C. Kelley, "Predictors of extensive subclinical spread in nonmelanoma skin cancer treated with Mohs micrographic surgery," Arch. Dermatol. **138**(8), 1043–1051 (2002).
8. J. A. Zitelli, C. Brown, and B. H. Hanusa, "Mohs micrographic surgery for the treatment of primary cutaneous melanoma," J. Am. Acad. Dermatol. **37**(2), 236–245 (1997).
9. C. P. Karakousis, C. M. Balch, M. M. Urist, M. M. Ross, T. J. Smith, and A. A. Bartolucci, "Local recurrence in malignant melanoma: long-term results of the multiinstitutional randomized surgical trial," Ann. Surg. Oncol. **3**(5), 446–452 (1996).
10. C. M. Balch, S. J. Soong, T. Smith, M. I. Ross, M. M. Urist, C. P. Karakousis, W. J. Temple, M. C. Mihm, R. L. Barnhill, W. R. Jewell, H. J. Wanebo, and R. Desmond, "Long-term results of a prospective surgical trial comparing 2 cm vs. 4 cm excision margins for 740 patients with 1-4 mm melanomas," Ann. Surg. Oncol. **8**(2), 101–108 (2001).
11. J. Cook and J. A. Zitelli, "Mohs micrographic surgery: a cost analysis," J. Am. Acad. Dermatol. **39**(5), 698–703 (1998).
12. E. Eisenberg, "Frozen section examination of the margins for resection of squamous cell carcinoma of the lower lip," J. Oral Maxillofac. Surg. **61**(8), 895–897 (2003).
13. M. E. Dawn, A. G. Dawn, and S. J. Miller, "Mohs surgery for the treatment of melanoma in situ: a review," Dermatol. Surg. **33**(4), 395–402 (2007).
14. G. Argenziano and H. P. Soyer, "Dermoscopy of pigmented skin lesions—a valuable tool for early diagnosis of melanoma," Lancet Oncol. **2**(7), 443–449 (2001).

#168187 - $15.00 USD Received 15 May 2012; revised 19 Jun 2012; accepted 19 Jun 2012; published 22 Jun 2012

15. H. Kittler, H. Pehamberger, K. Wolff, and M. Binder, "Diagnostic accuracy of dermoscopy," Lancet Oncol. **3**(3), 159–165 (2002).
16. M. Rajadhyaksha, M. Grossman, D. Esterowitz, R. H. Webb, and R. R. Anderson, "In vivo confocal scanning laser microscopy of human skin: melanin provides strong contrast," J. Invest. Dermatol. **104**(6), 946–952 (1995).
17. A. Gerger, S. Koller, W. Weger, E. Richtig, H. Kerl, H. Samonigg, P. Krippl, and J. Smolle, "Sensitivity and specificity of confocal laser-scanning microscopy for in vivo diagnosis of malignant skin tumors," Cancer **107**(1), 193–200 (2006).
18. C. L. Smithpeter, A. K. Dunn, A. J. Welch, and R. Richards-Kortum, "Penetration depth limits of in vivo confocal reflectance imaging," Appl. Opt. **37**(13), 2749–2754 (1998).
19. E. M. C. Hillman, D. A. Boas, A. M. Dale, and A. K. Dunn, "Laminar optical tomography: demonstration of millimeter-scale depth-resolved imaging in turbid media," Opt. Lett. **29**(14), 1650–1652 (2004).
20. S. A. Burgess, M. B. Bouchard, B. Yuan, and E. M. C. Hillman, "Simultaneous multiwavelength laminar optical tomography," Opt. Lett. **33**(22), 2710–2712 (2008).
21. B. Yuan, S. A. Burgess, A. Iranmahboob, M. B. Bouchard, N. Lehrer, C. Bordier, and E. M. Hillman, "A system for high-resolution depth-resolved optical imaging of fluorescence and absorption contrast," Rev. Sci. Instrum. **80**(4), 043706 (2009).
22. S. A. Burgess, D. Ratner, B. R. Chen, and E. M. C. Hillman, "Fiber-optic and articulating arm implementations of laminar optical tomography for clinical applications," Biomed. Opt. Express **1**(3), 780–790 (2010.
23. A. K. Dunn and D. A. Boas, "Transport-based image reconstruction in turbid media with small source-detector separations," Opt. Lett. **25**(24), 1777–1779 (2000).
24. L. Wang, S. L. Jacques, and L. Zheng, "MCML—Monte Carlo modeling of light transport in multi-layered tissues," Comput. Meth. Prog. Bio. **47**(2), 131–146 (1995).
25. I. V. Meglinski and S. J. Matcher, "Quantitative assessment of skin layers absorption and skin reflectance spectra simulation in the visible and near-infrared spectral regions," Physiol. Meas. **23**(4), 741–753 (2002).
26. W. F. Cheong, S. A. Prahl, and A. J. Welch, "A review of the optical properties of biological tissues," IEEE J. Quantum Electron. **26**(12), 2166–2185 (1990).
27. J. T. Whitton and J. D. Everall, "The thickness of the epidermis," Br. J. Dermatol. **89**(5), 467–476 (1973).
28. J. Feit, W. Kempf, H. Jedlicková, and G. Burg, "Hypertext atlas of dermatopathology with expert system for epithelial tumors of the skin," J. Cutan. Pathol. **32**(6), 433–437 (2005).
29. S. D. Konecky, A. Mazhar, D. Cuccia, A. J. Durkin, J. C. Schotland, and B. J. Tromberg, "Quantitative optical tomography of sub-surface heterogeneities using spatially modulated structured light," Opt. Express **17**(17), 14780–14790 (2009).
30. J. P. Culver, T. Durduran, D. Furuya, C. Cheung, J. H. Greenberg, and A. G. Yodh, "Diffuse optical tomography of cerebral blood flow, oxygenation, and metabolism in rat during focal ischemia," J. Cereb. Blood Flow Metab. **23**(8), 911–924 (2003).

1. Introduction

Skin cancer is the commonest form of cancer in the United States, with over one million new cases of non-melanoma and 81,000 new cases of melanoma expected in 2012 [1,2]. The most common treatment for malignant skin lesions is surgical resection. However, although non-melanoma skin cancer treatments typically have a high success rate, this outcome often requires excision of a significant margin around the lesion [3–7]. Since such lesions are commonly located on sun-exposed areas of the head, face and neck, excessive margin removal can be disfiguring [8–10]. Patients will often undergo initial conservative resection, but the wound will be left open for several days while margin histopathology is used to determine whether further resection is required, a process which can be very distressing [11,12]. Mohs surgery uses frozen tissue histology for faster results, but differences in surgical technique and laboratory facilities can lead to variable outcomes [13]. Melanoma lesions can be highly aggressive, leading to distant metastases if diagnosis and treatment are delayed. Metastasis is more likely if the tumor has thickened and invaded into the dermis, making evaluation of lesion thickness an important parameter for treatment planning [9]. Therefore, establishing an accurate clinical margin *in vivo*, prior to resection, both in lateral extent and in depth, could significantly improve treatment and reduce postsurgical morbidity in either type of skin cancer.

Clinical examination of any suspected skin lesion is typically performed visually under white light, allowing little perception of lesion depth. Biopsies are obtained to determine the exact nature of the lesion prior to resection, but these do not sample the full extent of the lesion. More advanced visualization approaches include dermoscopes; handheld devices that exploit polarization to reject superficially scattered light and specular reflection, enhancing appreciation of deeper portions of the epidermis [14]. However, while dermoscopes allow lesion color, boarder, and shape to be more clearly visualized compared to a standard white

#168187 - $15.00 USD Received 15 May 2012; revised 19 Jun 2012; accepted 19 Jun 2012; published 22 Jun 2012

light exam, since this device relies on the visual impression of the clinician, results depend heavily on training [15]. Another advanced technology for skin lesion evaluation is reflectance confocal microscopy [16,17]. This technique exploits refractive index mismatches between the nuclei and cytoplasm of cells to generate high-resolution, depth-sectioned images of the *in vivo* cellular architecture of skin. However, the penetration depth of this technique is less than 200 microns, limiting it to structures above and around the epidermal / dermal junction [18]. Its field of view is also typically small (<500 microns), requiring careful surveying of multiple sites rather than assessment of an entire lesion. Reflectance confocal is also not directly sensitive to the absorption properties of lesions, and therefore cannot distinguish lesion margins on the basis of pigment color or density.

Laminar Optical Tomography (LOT) is a strong complement to these existing methods, since it can provide sensitivity to deeper tissues, as well as to absorption contrast [19]. Here, we seek to demonstrate how LOT could be used to aid clinicians in their evaluation of skin cancer margins prior to surgical resection. LOT employs a configuration similar to a laser scanning confocal microscope, but utilizes an array of detectors at the de-scanned confocal plane (as compared to the single detector behind a pinhole in a standard confocal system) [20]. These detectors are imaged to positions up to 1.75 mm from the focus of the scanning beam and detect photons that have undergone progressively more scattering events compared to on-axis light. These photons have, on average, traveled through deeper tissues than their on-axis counterparts, enabling evaluation of optical contrast in progressively deeper regions within the tissue. Since scattered photons have traveled further within the tissue, they are more sensitive to absorption contrast. LOT uses three distinct laser wavelengths designed to evaluate optical absorption due to common tissue chromophores, specifically oxy- and deoxy-hemoglobin and melanin. This enables quantitative analysis of the distribution of chromophores at various depths, which are important in both pigmented (melanin) and nonpigmented (hemoglobin) skin lesions.

In this paper, we evaluate LOT as an adjunct tool for clinicians to aid in their assessment of skin lesions *in vivo*. We first present LOT data acquired from skin-like optical phantoms, and demonstrate a generalized method to predict a lesion's relative depth and thickness, depending on the detected intensity profile seen over the range of source-detector separations. Our generalized method is then applied to common, benign lesions in normal volunteers to distinguish between a likely junctional nevus and compound nevus. Finally, a clinical case study is discussed in which LOT is shown to resolve subepidermal neoplastic tissue not visible on white light photography.

2. Materials and methods

2.1 Laminar optical tomography

The optical configuration for LOT as utilized in this study can be seen in Fig. 1. Simply, collinearly aligned lasers at three wavelengths (488nm, 532nm, and 638nm) are directed through a polarizing beam splitter cube and onto scanning galvanometer mirrors. A scan lens and objective lens focus the raster scanning beam onto the tissue. Light returning from the tissue is de-scanned, passes through a 3-band dichroic beamsplitter and is then separated by a polarizing beam splitter. Light that has lost its initial polarization state is directed to the absorption detection arm (suppressing specular reflections). Here, light travels through a focusing lens and slit, then passes through a diffraction grating, where the three reflected wavelengths are differentially dispersed onto a 2-dimensional photomultiplier tube (PMT) array allowing simultaneous detection [19]. While not utilized here, the system also includes provision to measure fluorescence, separated by the 3-band dichroic and directed to the fluorescence detection arm, which contains a focusing lens, slit and linear PMT array [21].

Figure 1 depicts how detectors with larger lateral offsets will detect light that has undergone more scattering events and has, on average, traveled deeper through tissue. As the focused laser beam raster scans, each offset detector generates its own image corresponding to light emerging at different lateral distances from the scanning spot. The result is a data set

#168187 - $15.00 USD Received 15 May 2012; revised 19 Jun 2012; accepted 19 Jun 2012; published 22 Jun 2012

comprising a series of images where contrast is generated from increasingly deep structures. The clinical data shown in this study was acquired using an articulating arm providing positioning of the region of interest with three degrees-of-freedom [22].

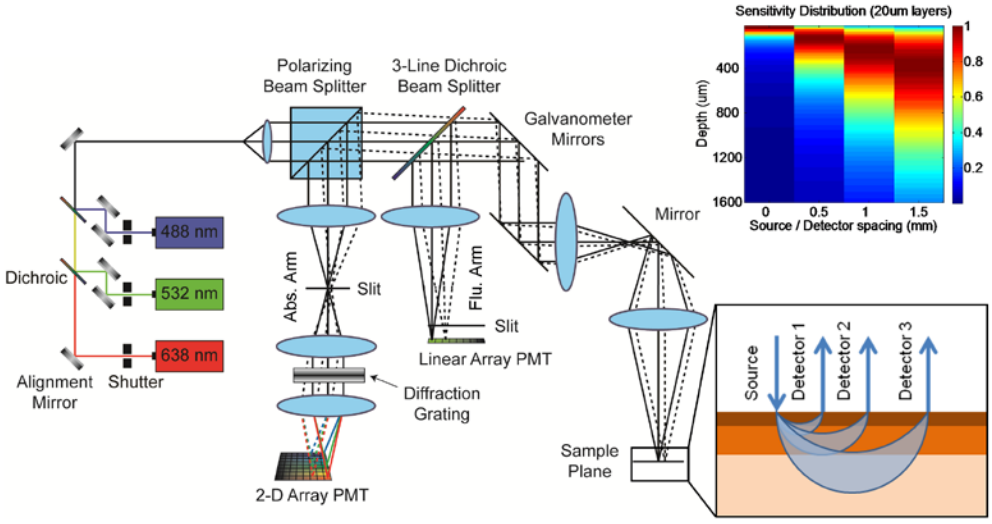

Fig. 1. Schematic diagram of Laminar Optical Tomography system. lower inset: illustration of offset detector geometry and average photon pathways in tissue (blue arcs). Note that wider detector offsets yield deeper average photon migration pathways. Upper inset: Monte Carlo-derived depth sensitivity of LOT measurements at four source-detector offset positions for optical properties approximating skin (normalized to 1 for each offset).

2.2 Monte Carlo modeling

The spatial sensitivity of LOT measurements can be predicted using a model of light propagation. Since LOT makes measurements over length scales of less than a few millimeters, close to the scattering length of typical tissue, diffusion models are inappropriate. We therefore chose to utilize Monte Carlo modeling. Our model is based on the work of Dunn et al, which in turn is a 3D, multi-region implementation of MCML code by Wang et al [23,24]. Modifications were made to ensure that photon visitation was recorded even when a photon did not scatter within a given voxel. Illumination was modeled as a single focused beam with a numerical aperture of 0.05. Simulations were then performed by allocating a series of equally spaced layers at increasing depths from the surface of the modeled volume, and recording the pathlength of each visiting photon within each layer. The position and direction of each photon exiting the modeled tissue was then recorded along with its respective total pathlength within each layer. Post-hoc analysis of this modeled data was then used to predict the relative sensitivity of photons emerging at different lateral distances from the incident beam to changes in absorption in each depth layer.

An example of the output from a skin-simulating model is shown inset in Fig. 1, which used 20 micron thick layers over 4000 microns of depth (the top 1600 microns are shown) for background optical properties of absorption coefficient μ_a = 0.2 mm^{-1}, scattering coefficient μ_s = 45 mm^{-1} (100 micron thick epidermis) and μ_s = 30 mm^{-1} (dermis) and anisotropy factor g = 0.8 [25–27]. The plot shows the total photon visitation pathlength in each layer for given source-detector separations (normalized to 1 for each separation). This demonstrates that, for these optical properties, 0 separation measurements are sensitive primarily to the upper 50-100 microns of skin, whereas a 0.5 mm separation is more sensitive to depths between 100 and 300 microns, a 1 mm separation; to 200-500 microns and a 1.5 mm separation; to 300-800 microns. This suggests that narrower separations will almost exclusively probe the stratum

#168187 - $15.00 USD Received 15 May 2012; revised 19 Jun 2012; accepted 19 Jun 2012; published 22 Jun 2012

corneum and epidermis (the top 100-200 microns in most human skin), while wider separations will be more sensitive to the papillary and deeper reticular dermis.

2.3 Phantom construction

To quantitatively compare Monte Carlo simulation results to real LOT measurements, phantoms were created using constructs composed of agarose (Acros Organics, 9012-36-6), 20% Intralipid (Sigma-Aldrich, I141), bovine hemoglobin (Sigma-Aldrich, H2500) and coffee powder (Medaglia D'Oro, to mimic melanin) in proportions to yield optical properties of μ_a = 0.2 mm^{-1}, μ_s = 4.0 mm^{-1}, and g = 0.8. Thin sheets of agarose (containing Intralipid, with or without 'melanin') were cast between two microscope slides spaced with two 200 micron thick cover glasses, and layered on top of an agarose-based 'dermis' containing Intralipid and hemoglobin [19]. This layering yielded phantoms with nevus-like absorbing inclusions of varying depths and thicknesses between 200 and 600 microns. Each phantom was prepared immediately before imaging to avoid dispersion of absorbers between layers. A photo of one such phantom is shown in Fig. 2(a).

2.4 LOT phantom imaging

LOT phantom data was acquired by positioning phantoms under the system's objective lens. A transparent ruler was placed onto the edge of the phantom to provide accurate measurements of field of view size and source-detector separations. Data was acquired in sets of 15 frames (300 by 300 pixels per frame) at 5 frames per second using the system's 532nm laser. Calibration of LOT data is dependent on many factors including the uniformity of illumination (L_s), the efficiency of detection ($E_{s,d}$), system reflections ($R_{s,d}$), the relative gains of each detection channel (g_d), and dark counts and ambient light (D_d) [21]. We can therefore describe the raw PMT signal for source position *s* and detector *d* ($M_{s,d}$) measured by LOT as:

$$M_{s,d} = E_{s,d} L_s g_d \left(S_{s,d} + R_{s,d} + D_d \right) \tag{1}$$

where $S_{s,d}$ is the desired signal from the sample. If we wish to consider only the relative change in signal (*differential contrast*) with respect to a reference region or object: $\Delta S/So$, we can cancel out all of these terms through subtraction of a "dark image" acquired by collecting a scan without any sample present at the focal plane (DI_{ns}):

$$DI_{s,d} = E_{s,d} L_s g_d \left(R_{s,d} + D_d \right) \tag{2}$$

$$Mo_{s,d} = E_{s,d} L_s g_d \left(So_{s,d} + R_{s,d} + D_d \right) \tag{3}$$

$$\Delta S / So = \left(M - Mo \right) / \left(Mo - \right) \tag{4}$$

In the case of skin imaging, $Mo_{s,d}$ is the signal extracted from a region of normal tissue adjacent to the lesion of interest. The analysis above shows that differential contrast $\Delta S/So$ is robust to many potential experimental errors. We demonstrate below using simulations and phantom measurements that the information content $\Delta S/So$ is also sufficient to yield information about the depth and thickness of absorbing lesions.

2.5 In vivo imaging of skin lesions

In vivo data was acquired under a protocol approved by the Institutional Review Board at Columbia University Medical Center. Patients were recruited for LOT imaging if they had a pigmented lesion greater than 1cm from their eyes and were scheduled for resection surgery. After initial white-light photography, a 1 cm by 1cm area including the lesion was imaged with the LOT at approximately 5 frames per second, for a total of 15 frames, each frame comprising 7 source-detector pairs in each of the red, green, and blue reflectance channels. Appropriate calibration scans were also taken each day in the clinic. Following imaging, the clinical margin was determined by the expert clinician (D.R., blinded to LOT results), and

#168187 - $15.00 USD Received 15 May 2012; revised 19 Jun 2012; accepted 19 Jun 2012; published 22 Jun 2012

surgical excision of the lesion was performed. Standard histology was then performed on the removed tissue. The orientation and slice location within each histology cassette were carefully recorded for subsequent correlation to LOT images.

Additional LOT data was acquired in normal volunteers with benign melanocytic nevi of either junctional or compound characteristics. These nevi were not resected, but are compared to standard library histology. Junctional nevi were identified by their pigmented yet macular appearance and are expected to have melanocytes (and therefore, pigment-containing melanosomes) constrained to the dermal-epidermal junction. Compound nevi are also pigmented, but exhibit a slightly raised appearance and commonly have melanocytes and melanosomes extending beyond the dermal-epidermal junction into the dermis.

For both phantom and *in vivo* data, the sets of 15 repeated scans were averaged prior to extraction of differential contrast measures from chosen regions of interest. Where data is shown as a red-green-blue merge, raw LOT images from the red, green and blue lasers were normalized to their maxima and merged into an R-G-B bitmap.

3. Results

3.1 Monte Carlo modeling and phantom imaging

Figure 2(b) shows raw LOT data acquired on a representative phantom, with regions of interest centered on 200, 400 and 600 micron deep 'lesions' (top to bottom rows). Differences between the various source-detector separations can be appreciated, in particular that the contrast of the shallow 'lesion' is more uniform throughout all source-detector separations, whereas the deeper lesion cannot be seen in the narrower separation images. Data was extracted from these raw LOT images by selecting small regions of interests as indicated, corresponding to the lesion and background in order to calculate differential contrast ($\Delta S/So$) as a function of source-detector separation. A Monte Carlo model of the agarose phantom considered 10 x 100 micron layers (total volume depth 4mm) with $\mu_s = 4.0\ mm^{-1}$, and $g = 0.8$, with $\mu_a = 0.2\ mm^{-1}$ in the background and simulated the phantom's absorbing inclusions as 200 micron thick layers with $\mu_a = 5.0\ mm^{-1}$.

Figures 2(d) and 2(g) show plots of this differential contrast from LOT data (solid lines) compared to equivalent results from our Monte Carlo simulations (dashed lines). Error bars show the standard deviation of $\Delta S/So$ measurements over the 15 frames acquired. While some differences owing to model accuracy are to be expected, the general trends of both sets of curves are consistent between LOT measurements and our model. To parameterize these trends, a power law fit to the data ($y = ax^b$) was performed (black dashed lines). In Figs. 2(e) and 2(h), the fit parameters "a" and "b" for each geometry are plotted on a coordinate system (with "a" as the ordinate and "b" as the abscissa). Trend-lines illustrate that inclusions of fixed thickness and increasing depth will move to the top of this coordinate space (higher b), while inclusions of fixed depth and increasing thickness move to the right along the ordinate (higher a). Fits for LOT phantom measurements are shown as triangles in this space, and their positions agree well with the measured phantom geometry in all cases.

#168187 - $15.00 USD Received 15 May 2012; revised 19 Jun 2012; accepted 19 Jun 2012; published 22 Jun 2012

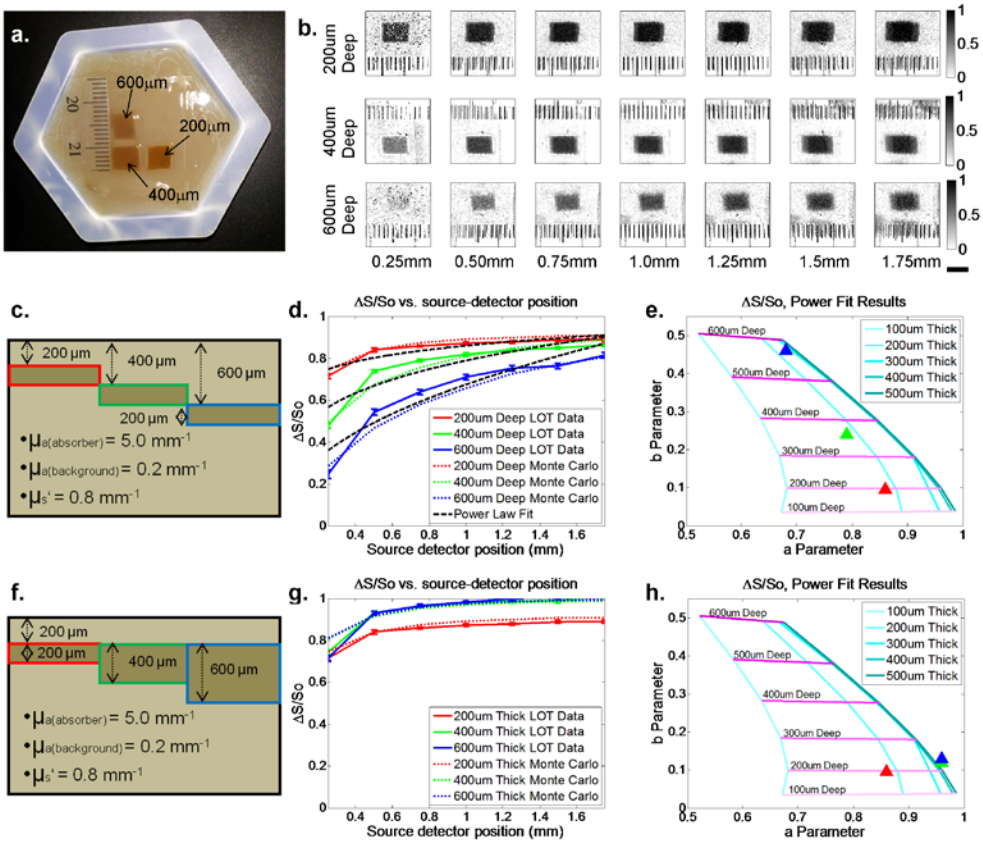

Fig. 2. Phantom and modeling results. (a) White light photograph of depth-varying optical phantom with the depth of each inclusion indicated. (b) Raw LOT phantom data inclusions of different depths displayed as differential contrast (ΔS/So). (c) and (f) Illustrations of depth-varying and thickness varying optical phantoms, respectively. (d) and (g) Differential contrast measured data (solid lines) and Monte Carlo simulation predictions (dashed lines) for lesions of different depths and thicknesses. Error bars show standard deviations of 15 repeated scans. Power law fits to experimental LOT data are also shown. RMS errors of these fits range from 0.0256 to 0.0666. (e) and (h) plots showing Monte Carlo-derived isolines of power law fit parameters '*a*' and '*b*' ($y = ax^b$), for various thickness and depths of inclusion. Triangles show results of the power law fits for phantom measurements from (d) and (g) respectively and agree well with phantom parameters. We note that compression of 'thickness' isolines at higher "a" values is a result of ΔS/So values approaching 1, corresponding to very little light reaching detectors. This is an intrinsic detection limit of LOT, since if light cannot reach the detector, it cannot distinguish between lesions of increasing thickness beyond that threshold.

While the optical properties and geometries of our phantoms are well-defined, the background optical properties and layered structure of human skin can be highly variable from person to person and on different parts of the body. To explore the sensitivity of our model and fitting technique to uncertainties in tissue optical properties, we simulated the effects of a 10% error in scattering coefficient on fit parameters "a" and 'b" for 200 micron thick lesions at three different depths for our phantom-like and skin-like models. Figure 3 shows that these changes have a relatively small effect on the predicted depth and thickness of the lesions and that, importantly, the trends across the plots for deeper and thicker lesions are maintained and robust against uncertainties in background optical properties. We note therefore that, given unavoidable uncertainties in background properties *in vivo*, that we do not expect our method to provide absolute quantitation of lesion thickness and depth, but rather relative measures of a lesion's thickness and depth that are robust and provide clinically useful information.

#168187 - $15.00 USD Received 15 May 2012; revised 19 Jun 2012; accepted 19 Jun 2012; published 22 Jun 2012

Below, we apply our analysis approach to LOT data acquired on *in vivo* lesions to obtain relative indicators of their depth and thickness.

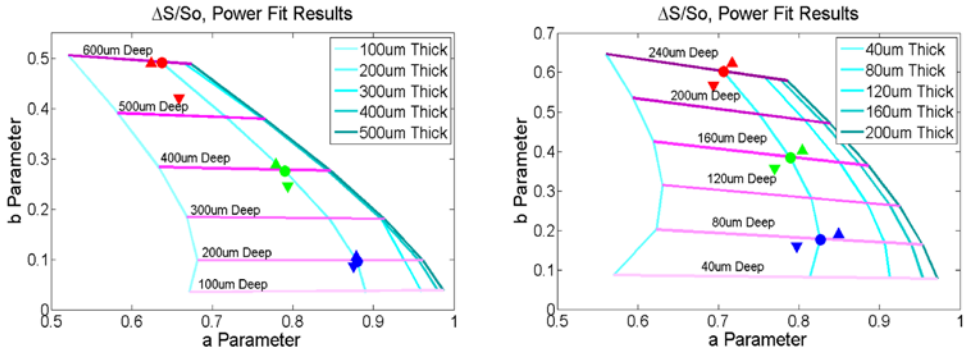

Fig. 3. Effects of background scattering properties on fit parameters. Filled circle represents the predicted fit parameters for an inclusion at the specified depth and thickness in (left) our phantom model (μ_a = 0.2 mm^{-1}, μ_s = 4.0 mm^{-1}, and g = 0.8) and (right) in our skin-like model (μ_a = 0.2 mm^{-1}, μ_s = 45 mm^{-1} (100 micron thick epidermis) and μ_s = 30 mm^{-1} (dermis) and g = 0.8). The colored triangles represent fit results when the background scattering coefficient is increased by 10% (upward pointing triangles) or decreased by 10% (downward pointing triangles). While the absolute prediction for each location changes somewhat, the trends related to relative depth and thickness are retained.

3.2 Normal volunteer: melanocytic nevus

The results of LOT imaging of benign melanocytic nevi are presented in Fig. 4. Two normal volunteers with apparent compound (Figs. 4(a)-4(c)) or junctional (Figs. 4(d)-4(f)) nevi were imaged with a standard white light camera (Figs. 4(a),4(d)) and LOT using the 532nm laser (Figs. 4(b),4(e)). Representative histopathology photomicrographs of these benign lesion types are shown (Figs. 4(c),4(f)) [28]. In compound nevi, nests of melanocytes can be seen at the dermal-epidermal junction and extending into the dermis (red arrows), while in junctional nevi, these nests are limited to the epidermal-dermal junction only. Since these cells produce the absorbing contrast (melanin containing melanosomes) to which LOT is sensitive, the power law fit technique was applied to analyze the physical properties of these skin lesions.

Figure 4(g) shows plots of differential contrast extracted from the raw LOT data regions indicated. The 'background' So measurement was extracted from a region of skin adjacent to the lesion (white box). Figure 4(d) shows the results of the power law fit to these curves plotted as triangles on top of our simulated parameter space (calculated using our skin-based Monte Carlo model with μ_a = 0.2 mm^{-1}, g = 0.8, μ_s = 45 mm^{-1} (epidermis) and μ_s = 30 mm^{-1} (dermis)). Consistent with our phantom results, the "a" and "b" parameters for the compound nevus suggest that it is thicker than junctional nevus, with both being shallow (superficial).

#168187 - $15.00 USD Received 15 May 2012; revised 19 Jun 2012; accepted 19 Jun 2012; published 22 Jun 2012

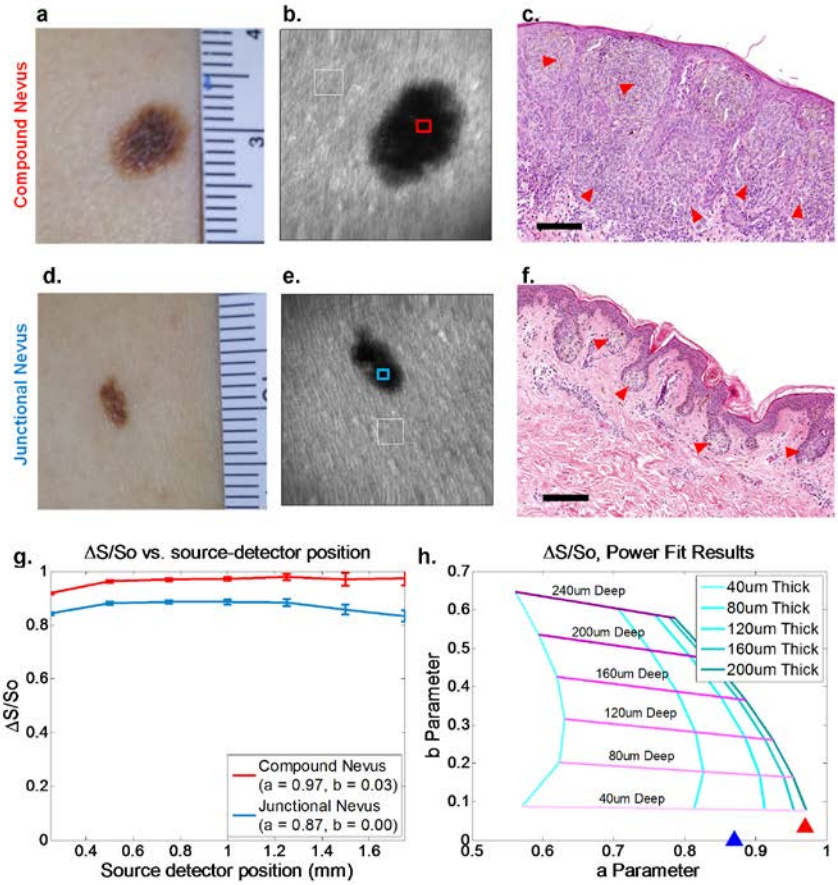

Fig. 4. LOT measurements of benign melanocytic nevi. (a),(d) White light images of Compound and Junctional nevi respectively. (b),(e) Raw LOT image (source-detector separation = 0.25mm) showing reference region (white box) and measurement region (red or blue box) for differential contrast calculation. (c),(f) Representative hematoxylin and eosin (H&E) histopathology images of junctional and compound nevi (40X) [28]. Scale bars approximately 100 microns. Arrowheads demonstrate location of melanocytes. Note that melanocytes in the compound nevus extend deep into the dermis, while melanocytes in the junctional nevus are limited to a thin region at the dermal – epidermal junction. (g), (h) LOT differential contrast and plot of fit parameters. Error bars show standard deviations of 15 repeated scans. RMS error of fit was 0.0096 and 0.0266 for the compound and junctional cases, respectively. Fit results are consistent with the compound nevus being substantially thicker than the junctional nevus, with both lesions being superficial.

3.3 Case study: squamous cell carcinoma

Figure 5 shows the results of LOT imaging on a 53-year-old male patient with a subsequently confirmed 9mm diameter squamous cell carcinoma present near the right nasolabial fold. The lesion had not been previously treated or biopsied. Surgical resection and histological analysis was performed following LOT data acquisition.

Figure 5(a) shows a white light image of the lesion taken with a standard digital camera. Figure 5(b) shows the same image with an RGB merged color LOT image superimposed to demonstrate the relative orientation of the two fields of view. A sequence of images showing the raw LOT data set for different source-detector separations is shown in Fig. 5(d). One of the most noticeable features of this data is the appearance, in wider source-detector separations, of a region that is strongly absorbing under blue and green illumination along one

#168187 - $15.00 USD Received 15 May 2012; revised 19 Jun 2012; accepted 19 Jun 2012; published 22 Jun 2012

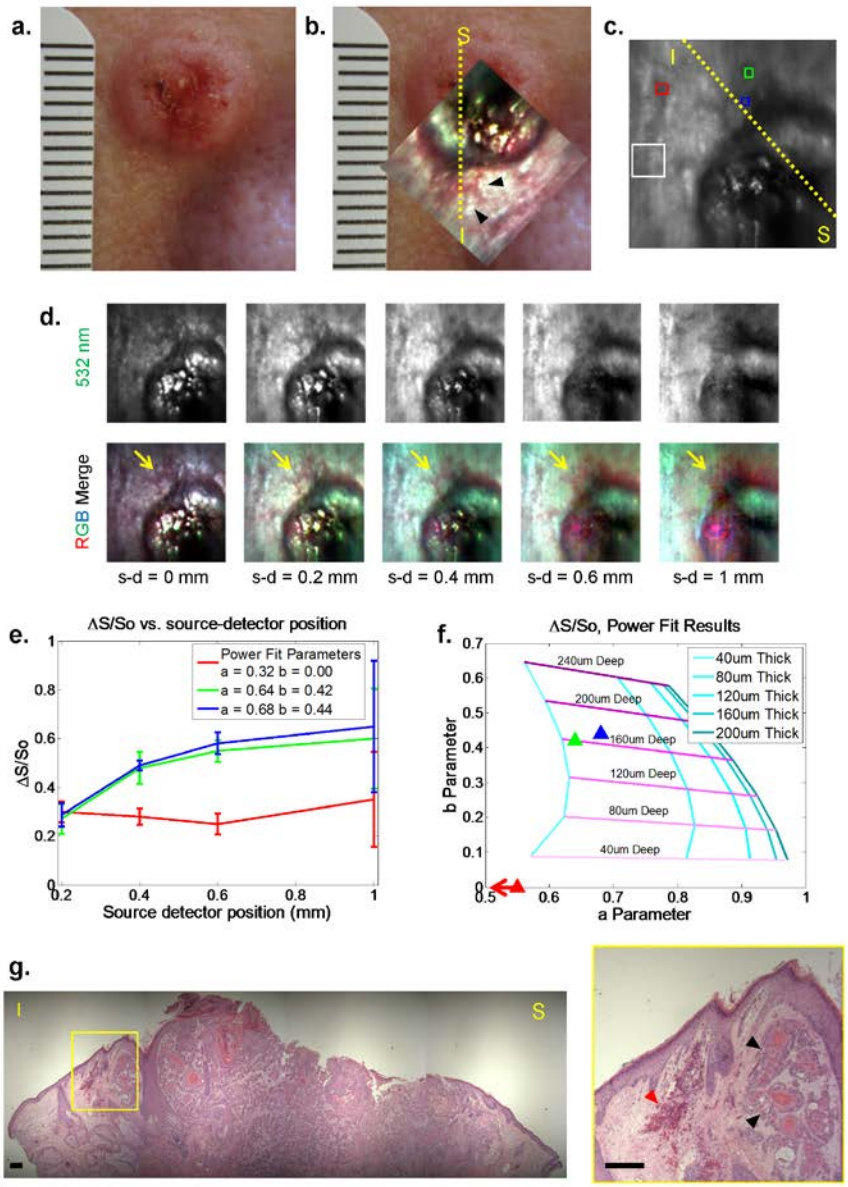

Fig. 5. Clinical squamous cell carcinoma. (a),(b) White light and LOT image at 0.20mm source-detector separation (inset) of squamous cell carcinoma lesion (metric ruler at left for scale). Yellow dashed line indicates approximate location of histopathology section from superior (S) to inferior (I) margins. (c) 532 nm LOT image showing regions of interest selected for differential contrast measurement. White box = reference region, Blue and green boxes = regions of interest. Red box = normal region. (d) Raw LOT frames taken at 532nm and RGB merged data for 5 source-detector (s-d) separations. Anomalous red structures are highlighted by yellow arrows (and black arrows in (b)). Note that the pink circles in wider separations are a specular reflection caused by the variable position of the articulating arm between imaging and calibration scans [21]. (e),(f) Plots of differential contrast and fit parameters of regions in (c). Error bars show standard deviations of 15 repeated scans. RMS error of fit for the red, green, and blue ROIs were 0.0462, 0.0528, and 0.0622, respectively. Note that the blue and green regions appear to be deeper than the red region (which is off scale to the left, implying a very superficial source of contrast). (g) H&E histopathology section from yellow dashed line. Scale bar 200 microns. Red arrowheads show increased subsurface blood accumulation, black arrowheads show adjacent aggregates of dysplastic keratinocytes.

#168187 - $15.00 USD Received 15 May 2012; revised 19 Jun 2012; accepted 19 Jun 2012; published 22 Jun 2012

edge of the lesion (appearing red in the RGB merge, indicated by yellow arrows). This region is not discernible from the rest of the lesion's perimeter in the white light photograph. Figure 5(c) shows regions of interest (ROIs) selected for differential contrast calculation; blue and green boxes were selected to target the regions of high blue and green contrast noted above, while the red box was selected from an assumed normal region. Only data from the 532nm laser was used for differential contrast calculation. The white box denotes the reference region (Mo), carefully chosen as a region with minimal apparent sub-surface structure. Figures 5(e) and 5(f) show the power law fit results for these regions overlaid on our skin-based simulated parameter space, suggesting that the blue and green regions appear to be both deep and fairly thick, while the region indicated by the red square in Fig. 5(c) is both thin and superficial, or essentially similar to the chosen reference region.

The histology section shown in Fig. 5(g) is approximately from the region indicated by yellow dashed line in the image in Figs. 5(b) and 5(c). This image shows a large central region comprising sheets of invasive dysplastic keratinocytes with occasional keratin pearls, without an overlying epithelium, indicative of an ulcer. Surrounding this ulcerated region, relatively normal-appearing epithelium is present. However, in the region highlighted by the yellow box (enlarged to the right) further keratin pearls and dysplastic keratinocytes are visible below the normal-appearing epithelium (black arrowheads). To the left of this, deposits of red blood cells indicative of dilated and leaky blood vessels are visible (red arrowhead). We believe that this hemoglobin-rich region is the origin of the 'deep' contrast seen in our LOT depth-dependent analysis. This contrast is not visible in the white light images of the lesion and likely represents an extension of the tumor margin and associated inflammation that is present below the normal-appearing surface epithelium of the area.

4. Discussion

In this paper we have demonstrated the potential of Laminar Optical Tomography to describe the depth and thickness of pigmented skin lesions, providing additional information compared to simple white light examination. This was achieved through the use of a simple power law fit of differential contrast versus source-detector separation. This method was developed and validated through the use of both Monte Carlo simulations and LOT data from skin-like phantoms. This fairly simplistic analysis approach was chosen to allow robust analysis of the relative depth and thickness of skin lesions, without the need for absolute knowledge of the background absorption and scattering structure of the tissue being imaged. As a result, our method is unlikely to provide truly quantitative measures, but rather relative measures of lesion thickness and depth that are of clinical value.

Our results suggest that LOT could become a useful adjunct tool for clinicians wishing to estimate the surgical margins and invasion depth of malignant skin lesions where preservation of normal tissue is paramount and treatment decisions must be made quickly. LOT offers the ability to probe relatively deep layers of tissue, and its sensitivity to hemoglobin and melanin make it ideal for detection of neoplasm-related angiogenesis in nonpigmented and pigmented lesions. We note that additional clinical measurements are required to demonstrate the true efficacy of LOT for this application.

One of the limitations of using LOT in its current form is adapting the optical setup for use in a clinical setting. Lesions may be present on any area of the body, and accessing these locations can be difficult. The articulating arm implementation of LOT used to acquire the clinical data shown here utilized rotation mounts and mirrors to provide a system capable of reaching a wide range of skin lesions quickly and effectively. However, this configuration suffered from problems related to correcting for specular reflections owing to the effects of polarization, and fiber optic bundle implementations of LOT have also proven problematic [22]. However, by incorporating newer technologies, we believe that LOT could be implemented in a number of simpler ways, including direct-contact arrays of sources and detectors exploiting miniature light emitting diode technology, or in hand-held configurations using microelectromechanical systems (MEMS) technology, either of which could substantially improve performance and reduce cost and complexity. Our results also

#168187 - $15.00 USD Received 15 May 2012; revised 19 Jun 2012; accepted 19 Jun 2012; published 22 Jun 2012

demonstrate the potential value to dermatology of ‘Modulated imaging’ and other wide field diffuse optical imaging approaches, which can yield equivalent data to LOT via projected spatial light patterns and camera-based detection [29,30].

Acknowledgments

This research was supported in part by the Wallace H. Coulter Foundation, the National Institutes of Health (R21NS053684, R01NS063226, R01NS076628, P30AR044535, R21AR059917 and U54CA126513) and the National Science Foundation (0954796 and GRFP funding for B. Chen). The authors also wish to thank Dr. George W. Niedt, MD for assistance with clinical histological analysis, and Dr Josef Feit, M.D., Ph.D., for permission to reproduce representative histology images shown in Fig. 4.

#168187 - $15.00 USD Received 15 May 2012; revised 19 Jun 2012; accepted 19 Jun 2012; published 22 Jun 2012